

Annual Review of Condensed Matter Physics
**Symmetry Breaking and
 Nonlinear Electric Transport in
 van der Waals Nanostructures**

Toshiya Ideue¹ and Yoshihiro Iwasa^{1,2}

¹Quantum-Phase Electronics Center (QPEC) and Department of Applied Physics,
 The University of Tokyo, Tokyo 113-8656, Japan; email: ideue@ap.t.u-tokyo.ac.jp

²RIKEN Center for Emergent Matter Science (CEMS), Wako, Saitama 351-0198, Japan;
 email: iwasa@ap.t.u-tokyo.ac.jp

Annu. Rev. Condens. Matter Phys. 2021. 12:201–23

The *Annual Review of Condensed Matter Physics* is
 online at conmatphys.annualreviews.org

<https://doi.org/10.1146/annurev-conmatphys-060220-100347>

Copyright © 2021 by Annual Reviews.
 All rights reserved

Keywords

van der Waals crystals, nanotube, nonreciprocal transport, electric-field-induced superconductivity, nonlinear Hall effect, photovoltaic effect

Abstract

The recent development of artificially fabricated van der Waals nanostructures makes it possible to design and control the symmetry of solids and to find novel physical properties and related functionalities. A characteristic physical property reflecting such symmetry breaking is the nonlinear response, which is typically studied as the second harmonic generation of light, although studies have recently expanded to include various transport phenomena. An important aspect of nonlinear transport for modern condensed matter physics is that it is not only a unique functionality of noncentrosymmetric systems but also an emergent property reflecting underlying physics such as spin-orbit interaction, superconductivity, magnetism, and band geometry/topology.

In this article, we review the nonlinear electrical transport in noncentrosymmetric van der Waals nanostructures obtained by exfoliation, nanostructure fabrication, or the application of an electric field, in particular, nonreciprocal transport resulting from inversion symmetry breaking and the bulk photovoltaic effect in nanomaterials without conventional p - n junctions.

ANNUAL
REVIEWS **CONNECT**

www.annualreviews.org

- Download figures
- Navigate cited references
- Keyword search
- Explore related articles
- Share via email or social media

1. SYMMETRY BREAKING IN SOLIDS AND VAN DER WAALS NANOSTRUCTURES

The effect of symmetry breaking on transport phenomena is a central issue in condensed matter physics. In general, symmetry breaking produces characteristic electronic, magnetic, or phononic states that are geometrical or topological in nature, resulting in novel transport in solids. To date, exotic transport originating from time reversal or spatial inversion symmetry breaking has been explored in linear regimes. Well-known examples include magnetotransport originating from the spin-splitting band or chiral-anomaly-induced negative magnetoresistance (1–15) and various spontaneous Hall effects (16–23). Nonlinear transport (24) has been recognized recently as a sophisticated probe of the effect of symmetry breaking on excitations in solids (**Figure 1a**).

When we apply an electric field E to a conducting material, the current, j , flowing in solids can be generally expressed as

$$j = \sigma^{(1)}E + \sigma^{(2)}E^2 + \sigma^{(3)}E^3 + \dots \quad 1.$$

The even-order terms, which vanish for centrosymmetric systems, owing to the symmetry requirements, appear only for noncentrosymmetric materials and thus directly reflect the effect of symmetry breaking on electronic transport.

Figure 1b,c shows schematics of the second-order nonlinear electric transport in solids. If the applied electric field is a dc field (or the frequency is low enough that it can be treated as a dc field), we simply call it nonreciprocal transport or unidirectional transport (**Figure 1b**) because the resistance depends on the sign of the current. By contrast, when the frequency of the applied electric field is high, it is called the bulk photovoltaic effect (**Figure 1c**), and it represents the emergence of a spontaneous photocurrent due to symmetry breaking. In both cases, the second-order nonlinear transport can be understood as the intrinsic rectification effect in the absence of a p - n junction.

Nanostructured systems of various materials offer new opportunities to control the structural symmetry, because their symmetries are often different from those of the bulk single crystals. In this context, van der Waals-layered materials provide a unique and rich opportunity, because the monolayer or few-layer forms, and even their heterostructures, which are called van der Waals interfaces, are easily obtained by exfoliation and various stacking techniques. These nanomaterials have different symmetries even though they are obtained from the same bulk material.

One of the most important systems is graphene (25), in which the electronic states can be dramatically changed by thinning it to a monolayer. Since the discovery of graphene, various two-dimensional (2D) materials including semiconductors, superconductors, magnets, and topological insulators (26–32), which show different properties from the bulk, have been investigated. Transition metal dichalcogenides (TMDs) with the 2H polymorph, for example, are a typical class of systems that exhibit broken inversion symmetry in the monolayer even though the bulk crystals are centrosymmetric (**Figure 2a**). Symmetry-reduced 2D electronic systems can also be obtained by applying a strong electric field at the surface (**Figure 2b**). In particular, the spin- and valley-related properties and functionalities of graphene and TMDs are attracting significant attention as unique features of these systems. In some cases, for example, bilayer graphene and TMDs, an electric field perpendicular to the 2D surface breaks the inversion symmetry in not only the out-of-plane direction but also the in-plane direction. Another interesting nanostructure is nanotubes (**Figure 2c**), as their cylindrical geometry and chirality affect the electronic states and transport properties (33, 34). Furthermore, researchers are now focusing on the symmetry at van der Waals interfaces (**Figure 2d**; 35–46). For example, the translational symmetry is dramatically modified by the moiré superlattice in twisted bilayer graphene and the hexagonal boron nitride (BN) heterostructure (39–42). Because van der Waals interfaces can be fabricated using any van der Waals

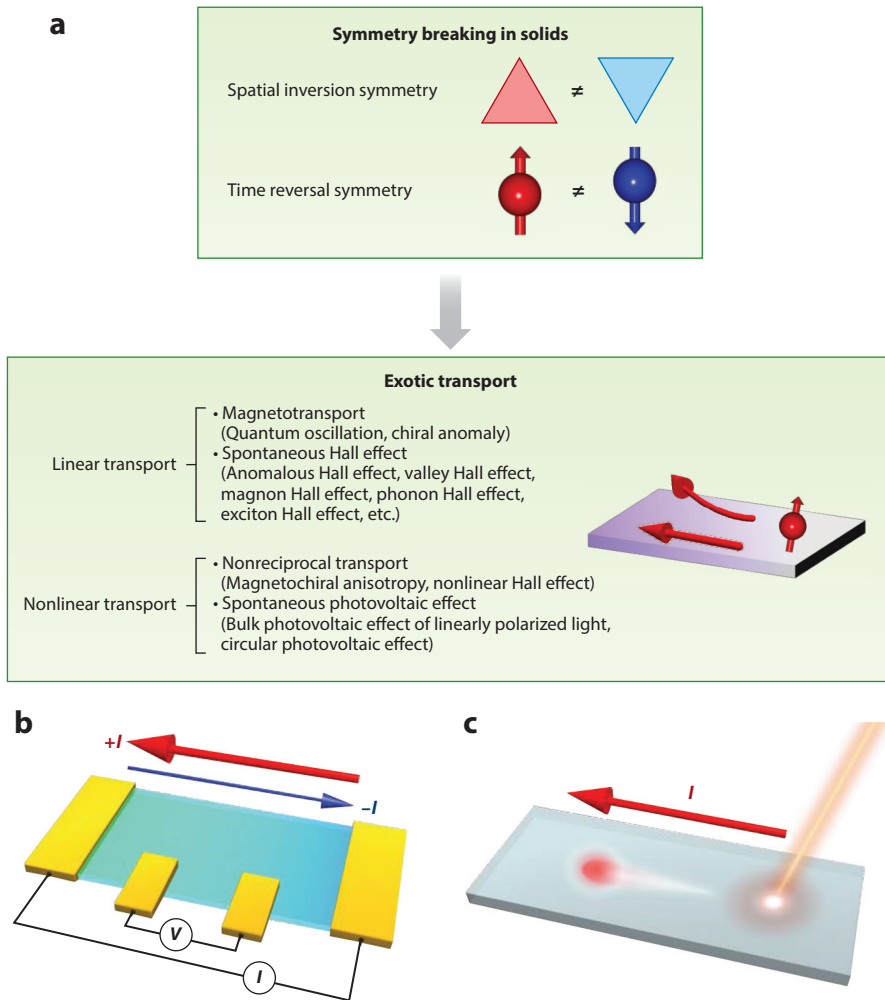


Figure 1

Effect of symmetry breaking on transport phenomena in solids (*a*) and nonlinear electric transport (*b,c*). (*a*) Quantum transport originating from symmetry breaking in solids. Some of the listed phenomena (quantum oscillations, the spontaneous Hall effect, the nonlinear Hall effect, the photovoltaic effect of linearly polarized light) require either time reversal symmetry breaking or spatial inversion symmetry breaking, and the others (chiral anomaly, magnetochiral anisotropy, the circular photovoltaic effect) require both. (*b*) Second-order nonlinear electric transport and (*c*) bulk photovoltaic effect. In addition to linear transport, nonlinear transport is an important probe of the symmetry breaking and exotic dynamics/properties of excitations in noncentrosymmetric systems, which are the main topic of this review.

materials, in any order, and with any stacking angle, irrespective of the lattice constant or lattice symmetry, we can freely design the symmetry of van der Waals interfaces to obtain other types of functional interfaces such as twisted TMDs with moiré superlattices (43–45) or strain-engineered graphene/black phosphorus heterostructure (46).

In this article, we review the nonlinear transport observed in various noncentrosymmetric van der Waals nanostructures. The characteristic behavior and microscopic mechanisms are presented, and future perspectives in this field are also discussed.

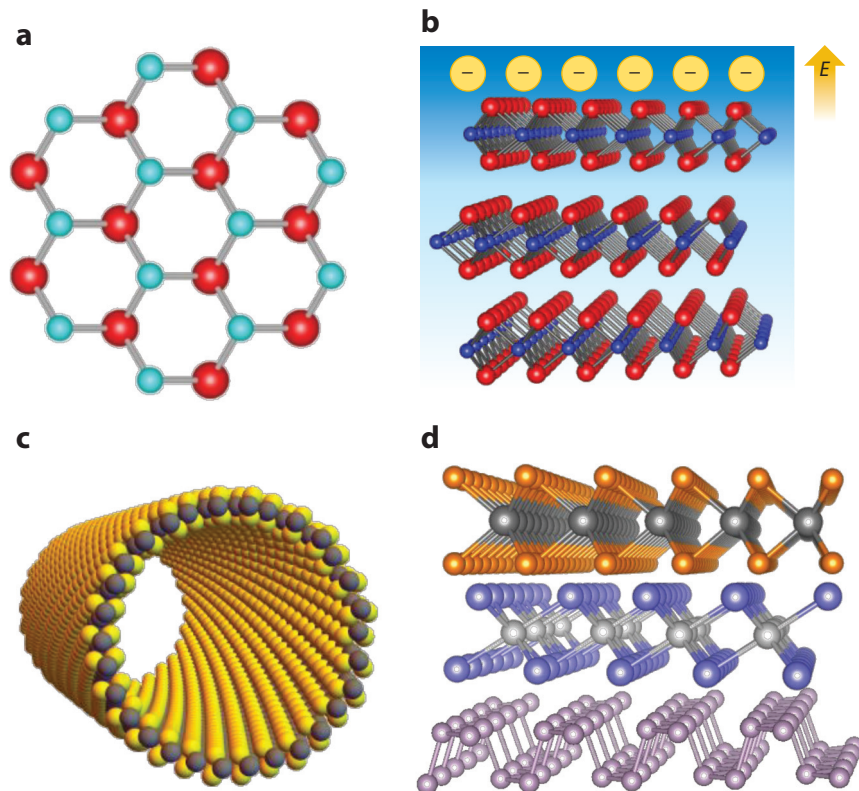


Figure 2

Symmetry breaking in van der Waals nanostructures. (a) Trigonal monolayer crystal, (b) reduced symmetry in multilayer crystal under electric field E , (c) nanotube, and (d) van der Waals interface.

2. NONRECIPROCAL TRANSPORT WITH BROKEN TIME REVERSAL SYMMETRY

In this section, we review the rectification effect realized under both spatial inversion and time reversal symmetry breaking. These phenomena were originally discussed by Rikken et al. (47) and are referred to as magnetochiral anisotropy. Rikken and colleagues have reported magnetochiral anisotropy in various materials such as the chiral Bi helix (47), carbon nanotubes (48), organic conductors (49), and the polar interface of silicon field-effect transistors (FETs) (50). In their original discussion, the electric resistance is empirically expanded up to the second order as a function of the current and magnetic field, which yields

$$R(I, B) = R_0(1 + \beta B^2 + \gamma IB). \quad 2.$$

In this formula, R_0 , I , and B represent the resistance at zero magnetic field, electric current, and external magnetic field, respectively. The second term on the right-hand side denotes the normal magnetoresistance, and the third term, which depends on both the electric current and magnetic field, corresponds to the magnetochiral anisotropy. In the following, we call it simply nonreciprocal transport. The current-dependent resistance generally causes a nonlinear voltage drop, which can be detected as the second harmonic signal in lock-in measurements. If we apply an ac input current ($I = I_0 \sin \omega t$), the nonlinear voltage or resistance due to the nonreciprocal transport can

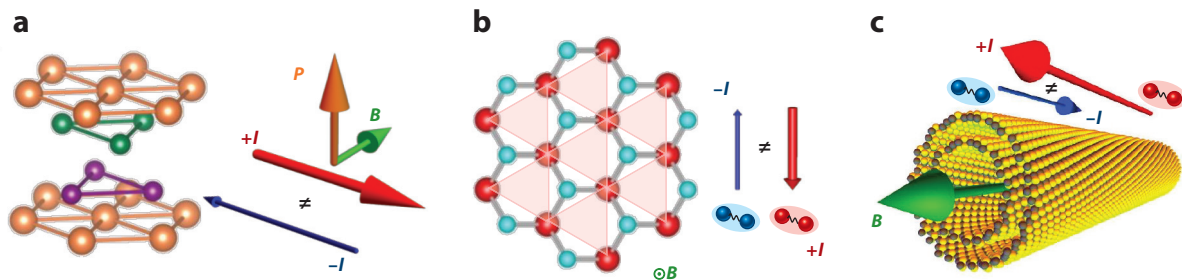


Figure 3

Nonreciprocal transport under magnetic field in noncentrosymmetric crystals. (a) Polar system, (b) trigonal system, and (c) chiral system. In each system, nonreciprocal transport satisfies the characteristic selection rule reflecting the symmetry breaking.

be expressed as follows:

$$V^{2\omega}(t) = \gamma R_0 B I_0^2 \sin^2 \omega t = \frac{1}{2} \gamma R_0 B I_0^2 \left[1 + \sin \left(2\omega t - \frac{\pi}{2} \right) \right] \quad 3.$$

$$R^{2\omega} \equiv \frac{1}{2} \gamma R_0 B I_0. \quad 4.$$

In centrosymmetric systems, the coefficient γ (generally a third-order tensor), which describes the ratio of the nonreciprocal resistance to the normal resistance, becomes zero. By contrast, γ is finite and satisfies the inherent selection rule reflecting the lattice symmetry in noncentrosymmetric systems. In the following section, we introduce the nonreciprocal transport observed in three types of noncentrosymmetric van der Waals nanostructures: polar, trigonal, and chiral systems (**Figure 3**).

2.1. Nonreciprocal Transport in Polar Systems

In polar systems with finite polarization \mathbf{P} , γ is finite when the magnetic field, electric current, and polar axis are perpendicular to each other (**Figure 3a**). Thus, the nonreciprocal resistance can be written as

$$R(I) - R(-I) \propto \mathbf{B} \cdot (\mathbf{I} \times \mathbf{P}) \propto BI \cos \theta, \quad 5.$$

where θ is the angle between the $\mathbf{I} \times \mathbf{P}$ direction and the magnetic field direction. Nonreciprocal transport originating from polar symmetry has been reported in various interface or surface systems (51–60) and bulk polar crystals (61, 62).

In **Figure 4**, we summarize the nonreciprocal transport in the bulk polar crystal BiTeBr (61). BiTeX ($X = \text{I, Br}$) is a polar van der Waals semiconductor composed of alternately stacked Bi, Te, and X layers (**Figure 4a**). The mirror symmetry along this stacking direction is broken, and the resultant Rashba-type spin splitting of the electronic bands has been confirmed by angle-resolved photoemission spectroscopy (63, 64). The transport signatures of the spin-split Fermi surface have also been reported as quantum oscillations in the resistance (65, 66) or thermoelectric coefficients (67). When an in-plane magnetic field is applied, the Rashba spin-splitting band is deformed along the direction perpendicular to the polarization and magnetic field, resulting in nonreciprocal transport (**Figure 4b**).

Figure 4c shows the second harmonic signals for $\theta = 0^\circ$ and 90° . When the magnetic field is perpendicular to the electric current ($\theta = 0^\circ$), a finite nonreciprocal resistance signal $R^{2\omega}$ appears

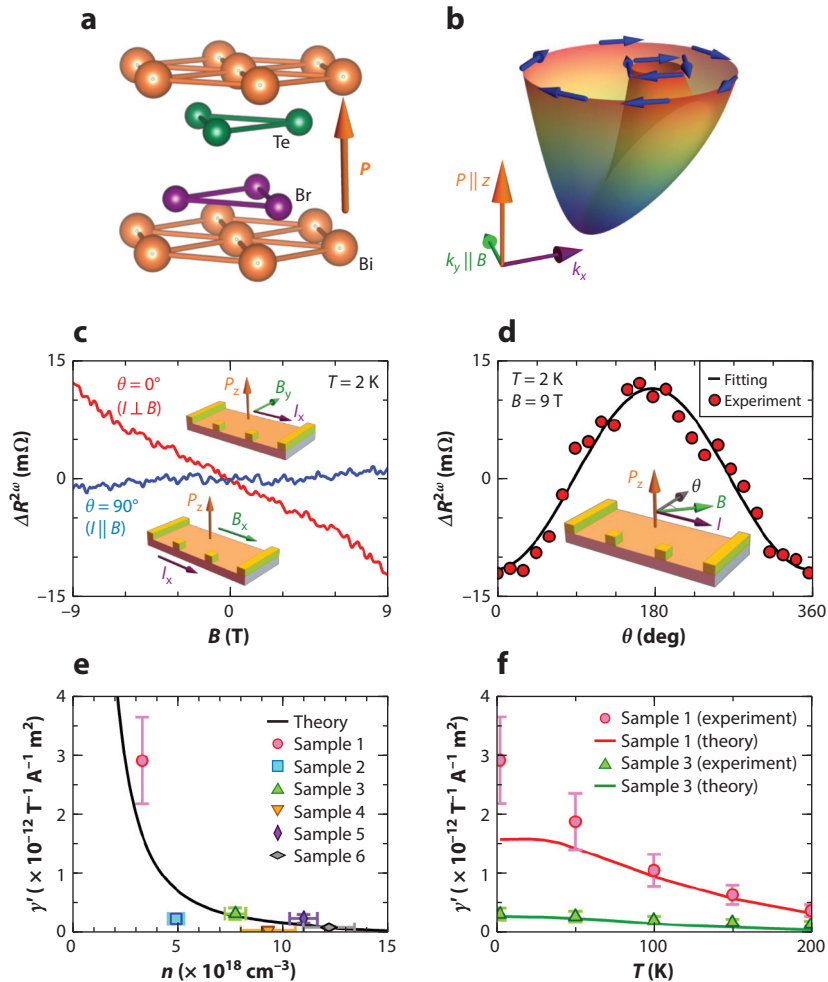


Figure 4

Nonreciprocal transport under magnetic field in polar crystal BiTeBr. (a) Crystal structure of BiTeBr. The mirror symmetry along the stacking direction is broken. (b) Schematics of band structure with Rashba-type spin-orbit interaction under magnetic field. Rashba spin-splitting band is deformed along the direction perpendicular to the polarization and magnetic field. (c) Second-order nonlinear magnetoresistance in two different configurations. (d) Angular dependence of nonreciprocal transport. The second-order nonlinear transport increases linearly with the magnetic field when the current is applied perpendicular to the magnetic field, whereas it is negligible when the current and magnetic field are parallel. (e) Carrier density dependence of nonreciprocal transport. (f) Temperature variation of nonreciprocal transport. The second-order nonlinear transport is greatly enhanced in low-carrier materials or at low temperature, which can be quantitatively explained by theoretical calculations. Figure adapted from Reference 61 with permission.

that is proportional to the magnetic field. ($\Delta R^{2\omega}$ indicates the antisymmetrized signal of $R^{2\omega}$ with respect to the magnetic field.) For $\theta = 90^\circ$, by contrast, the $\Delta R^{2\omega}$ signal is much smaller than that for the perpendicular configuration ($\theta = 0^\circ$). **Figure 4d** displays the θ dependence of $\Delta R^{2\omega}$ at $T = 2$ K and $B = 9$ T, which is well-fitted by a cosine curve. The selection rule and angular dependence in **Figure 4c,d** are reasonably consistent with Equation 5, indicating that this second harmonic signal demonstrates the nonreciprocal component of the resistivity. A particularly important feature

of this nonreciprocal response is its characteristic systematics; the magnitude of the nonreciprocal response is significantly enhanced with decreasing carrier density (**Figure 4e**) or decreasing temperature (**Figure 4f**). In these two panels, the vertical axes represent the normalized coefficient expressed as $\gamma' = \gamma L_y L_z$, where L_y and L_z are the sample width and thickness, respectively. It can be calculated theoretically as $\gamma' = -\frac{1}{B_y} \frac{\sigma_z}{(\sigma_1)^2}$ by using σ_1 and σ_2 in Equation 1. To date, nonreciprocal transport has been studied only qualitatively or in terms of a symmetry argument (47–50). However, the observed systematics shown in **Figure 4e,f** offers an unprecedented opportunity to elucidate the microscopic mechanism of the observed nonreciprocity quantitatively.

Here, we describe a theoretical model of the nonreciprocal transport in BiTeBr. We start from the three-dimensional Rashba Hamiltonian under a magnetic field along the in-plane (y) direction,

$$H = \frac{k_z^2}{2m_{\parallel}} + \frac{k_x^2 + k_y^2}{2m_{\perp}} + \lambda(k_x \sigma_y - k_y \sigma_x) - B_y \sigma_y \quad 6.$$

where m_{\parallel} (m_{\perp}) indicates effective mass along the direction parallel (perpendicular) to the polarization; σ_x , σ_y , σ_z are the Pauli matrices; and λ is the magnitude of the spin–orbit interaction. The first- and second-order nonlinear current along the x direction,

$$J_x = J_x^{(1)} + J_x^{(2)} = \sigma_1 E_x + \sigma_2 E_x^2, \quad 7.$$

can be calculated by solving the Boltzmann equation using the single relaxation time (τ) approximation.

We used the values of $\lambda = 2.00 \text{ eV}\mathring{\text{A}}$, $m_{\perp} = 0.15m_e$, and $m_{\parallel} = 5m_{\perp}$ (m_e is the electron mass in vacuum) for BiTeBr, which were obtained from previous studies, and calculated the coefficient γ' , as shown in **Figure 4e,f**. Despite the simplicity of the model, which takes only the B -induced band deformation into account and uses the single τ approximation, the agreement is excellent. This agreement is even more surprising when we recall that we did not use any fitting parameter in this calculation. More importantly, the magnitude of the nonreciprocal electric transport γ' was obtained considering only λ , m_{\perp} , and m_{\parallel} , which are the intrinsic band parameters, irrespective of the extrinsic parameter, the relaxation time τ . This indicates that the γ' parameter can be used to determine the band parameters, such as the Rashba splitting and effective mass of Rashba-type semiconductors. That is, the γ' parameter resembles the Hall coefficient, from which we can, in principle, determine the carrier density from transport measurements without any disturbance by extrinsic effects such as scattering. The above results for the Rashba-type semiconductor BiTeBr offer not only a microscopic understanding of intrinsic bulk rectification in polar conductors but also a simple electrical means of estimating the spin–orbit parameter of various noncentrosymmetric systems.

2.2. Nonreciprocal Transport in Noncentrosymmetric Trigonal Superconductors

Nonreciprocal transport can generally be expected to occur not only in the normal metallic state but also in exotic quantum phases such as superconductivity. In this section, we focus on the nonreciprocal superconducting transport in the trigonal 2D superconductor MoS₂.

MoS₂ is a semiconducting layered TMD. In the bulk form, it shows centrosymmetric 2H structures (**Figure 5a**). However, when it is exfoliated into a monolayer (**Figure 2a**), inversion symmetry is broken, resulting in D_{3h} symmetry. This trigonal symmetry in the monolayer produces characteristic orbital, spin, and valley properties in the TMD monolayers, such as a valley-dependent

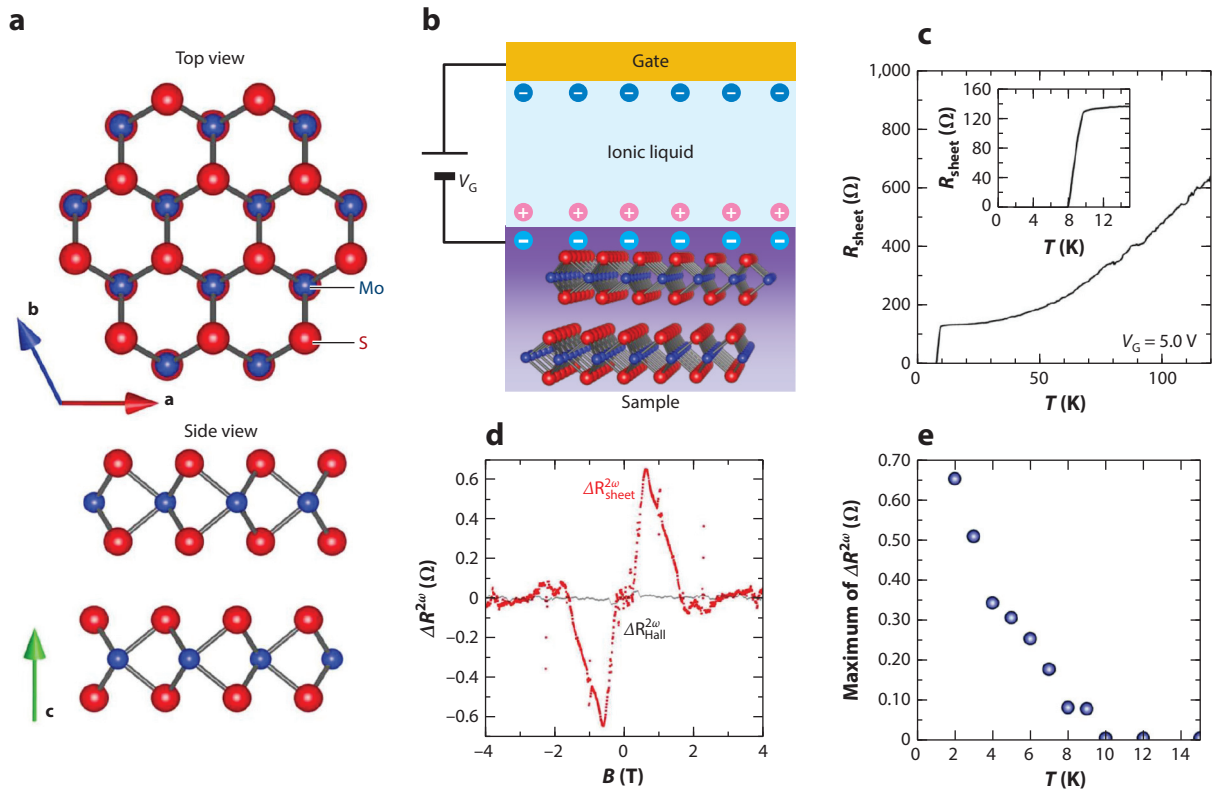


Figure 5

Nonreciprocal transport under magnetic field in trigonal superconductor MoS₂. (a) Crystal structure of 2H-MoS₂. (b) Schematic of ionic liquid gating on van der Waals microflakes. When a gate bias is applied, an electric double layer is formed at the interface between the ionic liquid and van der Waals crystals, which produces a quasi-2D electron system. (c) Electric-field-induced superconductivity in MoS₂. (d) Second-order nonlinear magnetoresistance in superconducting region. Longitudinal $\Delta R_{\text{sheet}}^{2\omega}$ shows the peak structure, whereas transverse $\Delta R_{\text{Hall}}^{2\omega}$ is almost absent. (e) Temperature variation of peak value of $\Delta R_{\text{Hall}}^{2\omega}$, which is greatly enhanced below the temperature in the superconducting region. Figure adapted from Reference 79 with permission.

optical transition, out-of-plane spin splitting with Zeeman-type spin-orbit interaction, and various Berry-curvature-related phenomena (68–71).

To fabricate trigonal 2D superconductors, we use an electric double-layer transistor (EDLT) on multilayer MoS₂. An EDLT is a type of FET in which the solid gate insulator in conventional FETs is replaced with an electrically insulating but ionically conducting substance, such as an electrolyte or ionic liquid (72). A schematic of the EDLT device is given in **Figure 5b**. When a gate voltage is applied between the top gate electrode and the source electrode attached to the semiconductor, high-density 2D carriers can accumulate on the channel surface of the semiconductors. The carrier density reaches the order of 10^{14} cm⁻², which is high enough to induce an insulator-to-metal transition and ultimately superconductivity (73–75).

When an EDLT is applied to multilayer MoS₂, the carriers are accumulated almost on the top-most layer of the MoS₂, and the symmetry is reduced to C_{3v} symmetry. At the same time, superconductivity is realized within the thickness of this 2D monolayer level (1 nm or less). Therefore, the gated MoS₂ can be regarded as a trigonal 2D superconductor in which the in-plane inversion symmetry is broken. Interestingly, a signature of noncentrosymmetric superconductivity has

already been observed as an enhancement of the in-plane upper critical field, which was attributed to spin–valley locking (76–78). In the following, we demonstrate that nonreciprocal transport also plays an important role in detecting the features of noncentrosymmetric superconductors.

Figure 5c shows the temperature dependence of the resistance of the EDLT-MoS₂ at a gate voltage V_G of 5.5 V. The superconducting transition, which is defined in terms of the half-value of the sheet resistance R_{sheet} in the normal state, was observed around $T = 9.8$ K. The antisymmetrized second harmonic magnetoresistance $\Delta R^{2\omega}$ as a function of the magnetic field in the superconducting state ($T = 2$ K) is displayed in **Figure 5d**. Nonreciprocal transport was clearly observed along the longitudinal zigzag direction, as shown by $\Delta R_{\text{sheet}}^{2\omega}$, whereas it was negligibly small along the transverse armchair direction ($\Delta R_{\text{Hall}}^{2\omega}$). This selection rule is consistent with the trigonal symmetry. In contrast to the nonreciprocal transport in the normal state discussed in the previous section, where the second harmonic signal increases in proportion to the magnetic field, $\Delta R_{\text{sheet}}^{2\omega}$ shows a nonmonotonous peak structure around the critical magnetic field in the superconducting MoS₂. When the magnetic field exceeds the upper critical field, the nonreciprocal signal is quickly quenched, indicating that the nonreciprocal response is significantly suppressed in the normal state. Suppression of the nonreciprocal signal $\Delta R_{\text{sheet}}^{2\omega}$ in the normal state appears more clearly in the temperature dependence of $\Delta R_{\text{sheet}}^{2\omega}$ plotted in **Figure 5e**. The nonreciprocal signal increases sharply when the system enters the superconducting phase. In terms of the symmetry, nonreciprocal transport is also allowed in the normal state, indicating that the nonreciprocal signal in the superconducting state is enhanced by orders of magnitude compared with that in the normal state.

Wakatsuki et al. (79) theoretically analyzed the nonreciprocal transport in a 2D trigonal superconductor. They used the Hamiltonian around the K and $-K$ points (80, 81),

$$H_{k\sigma\tau} = \frac{\hbar^2 \mathbf{k}^2}{2m} + \tau_z \Delta k_x (k_x^2 - 3k_y^2) - \Delta_Z \sigma_z - \Delta_{\text{SO}} \sigma_z \tau_z, \quad 8.$$

which well describes the conduction band edges of 2D MoS₂, and considered the second-order nonlinear current in both the normal and superconducting regions. In the above Hamiltonian, \hbar , m , and Δ represent the reduced Planck constant (Dirac constant), effective mass, and trigonal warping parameter (which describes the trigonal band deformation of the parabolic band reflecting the lattice potential), respectively; Δ_Z and Δ_{SO} are the spin splittings due to the Zeeman effect and the spin–orbit interaction, respectively; and $\sigma_z = \pm 1$ (or \uparrow, \downarrow) and $\tau_z = \pm 1$ (or $+, -$) represent the spin and valley degrees of freedom, respectively.

In the normal state, nonreciprocal transport is caused by the deformation of the spin-splitting band, similar to the case of polar semiconductors. By contrast, in the superconducting fluctuation state around T_c (where T_c is the superconducting transition temperature), following the analysis of the time-dependent Ginzburg–Landau equation, Wakatsuki et al. obtained the excess current resulting from the superconducting fluctuation, which is called the paraconductivity, as

$$\mathbf{j} = \frac{e^2}{16\hbar} \left(\frac{T - T_c}{T_c} \right)^{-1} \mathbf{E} - \frac{\pi e^3 m \Lambda B}{64 \hbar^3 k_B T_c} \left(\frac{T - T_c}{T_c} \right)^{-2} \mathbf{F}(\mathbf{E}). \quad 9.$$

Here, $\Lambda = \frac{93\zeta(5)}{28\zeta(3)} \frac{g\mu_B \Delta_{\text{SO}} \Delta}{(\pi k_B T_c)^2}$ [where $\zeta(s)$, g , k_B , and μ_B are the Riemann zeta function, g -factor, Boltzmann constant, and Bohr magneton, respectively], and $\mathbf{F}(\mathbf{E}) = (E_x^2 - E_y^2, -2E_x E_y)$ (79). The second term of Equation 9, which represents the nonreciprocal transport, satisfies the selection rule of the C_{3v} point group (**Figure 3b**), which has been observed experimentally (**Figure 5d**).

As a result of the energy scale difference between the superconducting and normal states, the ratio of the γ values in the normal region (γ_N) and the resistive superconducting region (γ_S) can

be estimated as

$$\frac{\gamma_S}{\gamma_N} \sim \left(\frac{\varepsilon_F}{k_B T_c} \right)^3, \quad 10.$$

where ε_F is the Fermi energy in the normal state. Because the Fermi energy is on the order of 100 meV, which is more than two orders of magnitude larger than T_c , γ_S/γ_N can be estimated as $\gamma_S/\gamma_N \sim 10^6$, which is consistent with the undetectable signal in the normal state in **Figure 5e**. The large enhancement of the γ parameter is expected to be a universal feature of noncentrosymmetric superconductors because it is derived from the general energy scale difference between the Fermi energy and the superconducting gap.

In the above discussion of the nonreciprocal superconducting transport, only the effect of the paraconductivity, which originates from the amplitude fluctuation of the superconducting order parameter, is considered (79, 82). However, it is well known that the thermally excited vortices and antivortices play dominant roles in the finite resistivity at approximately the Kosterlitz–Thouless (KT) transition temperature, $T_{KT} < T$. In addition, it was recently recognized that a temperature-independent resistive state appears in relatively clean 2D superconductors even far below the transition temperature when an out-of-plane magnetic field is applied (83, 84). This metallic state is interpreted in terms of a vortex liquid state as a ground state and is sometimes called a quantum metallic state (85). In light of this vortex picture, we should consider the effect of symmetry breaking on the vortex dynamics (86, 87). In a 2D trigonal superconductor, for example, vortex ratchet motion caused by the lattice asymmetry may cause nonreciprocal transport. Indeed, the vortex ratchet effect has already been reported in studies of superconducting films with artificial asymmetric potentials (88–91). This ratchet effect is well understood as a classical ratchet. However, in the quantum metallic state of 2D superconductors, the quantum creep of the vortex lattices is considered to be dominant and causes quantum ratchet motion of the vortices. Because it is known that ratchet rectification is suppressed in the quantum region and enhanced in the classical region (92), we can potentially determine whether the vortex motion is quantum or classical simply from the magnitude of the nonreciprocal transport. In a latest work (86), we successfully observed a change in the magnitude of the nonreciprocal transport in specific temperature and magnetic field regions, which potentially indicates a crossover between quantum and classical ratchets. Such a crossover was also theoretically discussed in Reference 93. Thus, nonreciprocal responses are extremely useful for elucidating the nature of the ground state of 2D superconductors.

2.3. Nonreciprocal Transport in Chiral Superconductors

Nonreciprocal transport is expected in chiral objects when a magnetic field is applied parallel to the current (**Figure 3c**); the resistance difference between the forward and backward directions can be written as

$$R(I) - R(-I) \propto \mathbf{B} \cdot \mathbf{I}. \quad 11.$$

It has been observed in the normal state in helical Bi (47), carbon nanotubes (48), an organic conductor (49), chiral magnets (94, 95), and elemental Te (96–98). It was also discovered recently in superconducting chiral WS_2 nanotubes (99, 100).

The samples used in Reference 99 were semiconducting multiwalled WS_2 nanotubes. **Figure 6a** shows a transmission electron microscopy (TEM) image of a WS_2 nanotube. The typical tube diameter is approximately 100 nm, and the number of layers is approximately 20. According to the literature (101–103), the tube part has a 2H structure. The electron diffraction pattern in **Figure 6b** suggests that different walls of the tube can have different chirality. In

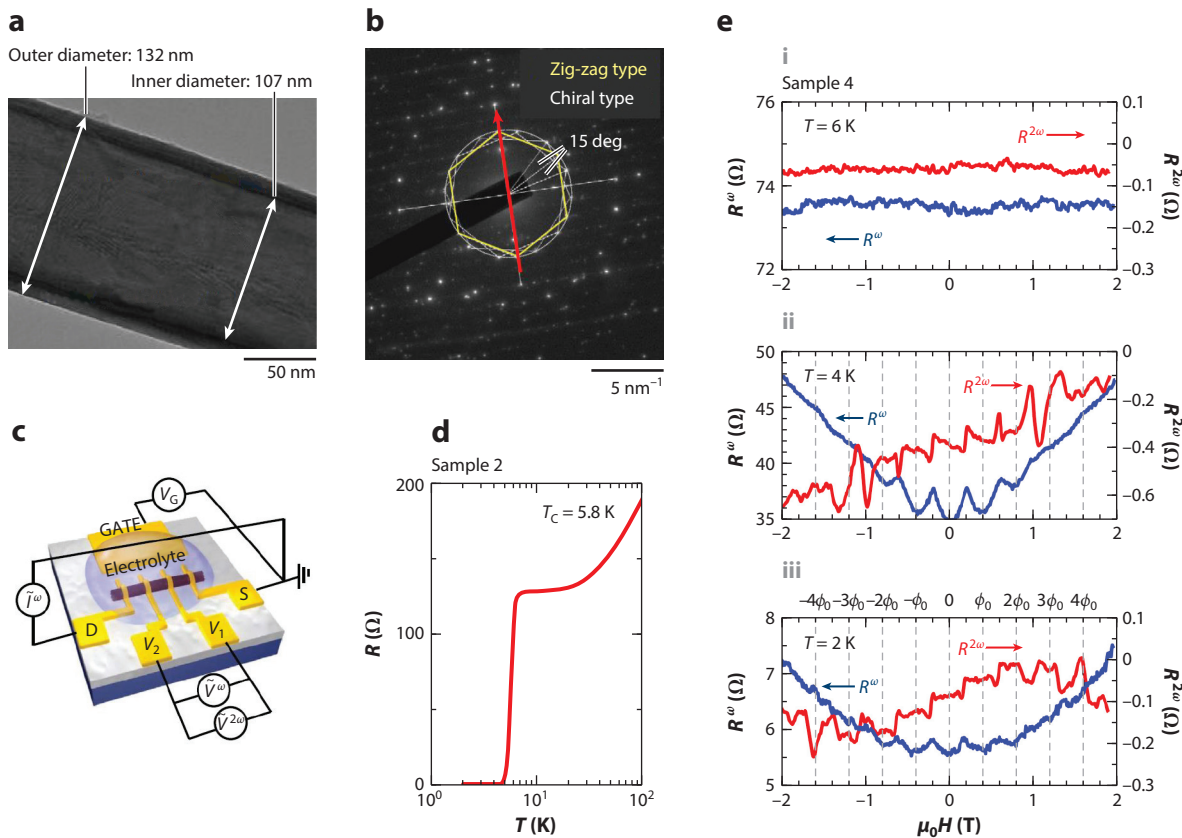


Figure 6

Nonreciprocal transport under magnetic field in superconducting chiral WS₂ nanotube. (a) Transmission electron microscopy image of WS₂ nanotube. Scale bar represents 50 nm. Sample is a multiwalled nanotube with diameter of approximately 100 nm. (b) Electron diffraction pattern of WS₂ nanotube. Scale bar represents 5 nm⁻¹. Nanotubes have a chiral component represented by pairs of tilted hexagons. (c) Schematic of electrolyte gating on an individual WS₂ nanotube. Unlike in the case of an electric double-layer transistor, ions are electrochemically intercalated into the layers. GATE, S, and D in the figure indicate the gate, source, and drain electrode, respectively. (d) Electric-field-induced superconductivity in WS₂ nanotube. (e) First and second harmonic magnetoresistance at $T = 6$, 4, and 2 K, respectively. In both the first and second harmonic magnetoresistance, periodic oscillating behavior is observed in the superconducting state. Figure adapted from Reference 99 with permission.

addition to the contribution of the zigzag-type nanotube, we see a pair of tilted hexagonal patterns, which confirms the coexistence of different chiral structures in this nanotube.

Individual nanotube devices (**Figure 6c**) were fabricated, and a KClO₄/polyethylene glycol electrolyte was used as the gate medium. By using this electrolyte instead of an ionic liquid as described in the previous section, we can realize the electrochemical intercalation of potassium ions into the interlayer space, which results in a higher-density carrier accumulation not only at the surface but also in the bulk (104, 105). **Figure 6d** shows the temperature dependence of the resistance of the WS₂ nanotube in the electrochemical intercalation region (V_G is set to 8 V). It exhibits metallic behavior, and superconductivity (defined as a decrease in the resistance to half of the normal-state resistance) appears at $T_c = 5.8$ K (**Figure 6d**). In contrast to the K-intercalated 2D WS₂ multilayer with $T_c = 8.6$ K (104), the superconducting transition of the K-intercalated WS₂ nanotube is shifted to a lower temperature and considerably broadened, possibly owing to

geometrical effects such as the curvature or reduced dimensions (100) or disorder arising from the incommensurability between different walls.

The magnetoresistance and nonreciprocal transport in this superconducting chiral WS₂ nanotube around T_c are studied in detail. **Figure 6e** shows the first and second harmonic resistances at $T = 6$ K, 4 K, and 2 K (*subpanels i, ii, and iii*, respectively). Here, the first harmonic resistance R^ω is physically identical to the normal magnetoresistance R . At $T = 6$ K, which is above T_c , the magnetoresistance is low. By contrast, at $T = 4$ and 2 K, the resistance at zero magnetic field decreases in accordance with the superconducting transition, and oscillating behavior is observed when the magnetic field is applied parallel to the tube axis. This oscillation during the superconducting transition is known as the Little–Parks (LP) effect (106) and originates from the interference of the superconducting current along the nanotube circumference and the resulting oscillation of T_c . In this situation, the total flux piercing the nanotube should have a quantized value of $N\phi_0 = Nb/2e$ (where b and e represent the Planck constant and charge of the electron, respectively, and N is an integer representing the number of flux quanta). The flux causes the oscillation of the free energy and the resulting oscillation of the resistance at a period of $\phi_0 = b/2e$. From the period of the LP oscillations, $\Delta(\mu_0 H)$, the effective diameter, d , of the superconducting nanotube can be estimated as 80 nm according to the relation $\frac{\Delta(\mu_0 H)\pi d^2}{4} = \frac{b}{2e}$, which is consistent with the TEM image (**Figure 6a**). These results confirm that superconductivity is realized in the tubular region of the WS₂ samples.

During the superconducting transition, nonreciprocal transport, which consists of the antisymmetric components of the second harmonic magnetoresistance as a function of the magnetic field, is enhanced. (Note that the second harmonic resistance is not antisymmetrized in **Figure 6e**; thus, $R^{2\omega}$ is not zero at zero magnetic field.) The observation of nonreciprocal transport in this configuration indicates unidirectional electrical transport due to the chiral symmetry. The observed $R^{2\omega}$ signal has two characteristic structures: the broader antisymmetric components and periodically oscillating terms in the low-magnetic-field region. The broader antisymmetric component is similar to the second harmonic magnetoresistance of MoS₂ discussed in the previous section. The oscillating terms show, by contrast, the same period, ϕ_0 , as the LP oscillations in the first harmonic magnetoresistance, which implies that they both have the same origin. Interestingly, this term shows stepwise behavior at 2 K (**Figure 6e, subpanel iii**), in contrast to the typical linear relationship with respect to the external magnetic field. These results indicate that the nonreciprocal supercurrent is also an interference current and is affected by the flux quanta passing through the nanotube.

The above result was the first discovery of superconductivity in an individual nanotube. The observation of the LP oscillation and nonreciprocal transport provided unambiguous evidence that superconductivity occurs in tubular and chiral objects, respectively. Consideration of the microscopic mechanisms of the nonreciprocal superconducting transport in terms of both vortex matter and paraconductivity remain as future work. Particularly in the latter, an anomalous pairing state or parity mixing, which reflects the chirality, should be an intriguing issue. The results for the WS₂ nanotube indicate that nonlinear transport is also an excellent probe for identifying and investigating exotic superconductivity in nanomaterials other than 2D systems.

3. NONLINEAR TRANSPORT UNDER TIME REVERSAL SYMMETRY

In the previous section, nonreciprocal transport in noncentrosymmetric systems under broken time reversal symmetry was discussed. However, second-order nonlinear transport can also occur even under time reversal symmetry. In this section, we focus on such nonlinear transport without a magnetic field nor magnetic ordering. Although it is expected to reflect the detailed band

topology/geometry or the exotic dynamics of excitations in solids, as nonreciprocal transport with broken time reversal symmetry does, nonlinear transport under time reversal symmetry has been studied only in recent years. In the following, theoretical prediction of nonlinear transport and experimental observation of the nonlinear Hall effect in WTe_2 are introduced.

3.1. Theory of Nonlinear Transport Under Time Reversal Symmetry

Nonlinear transport under time reversal symmetry has been theoretically discussed or proposed in several works (107–111). For example, nonlinear transport originating from anisotropic band structure or scattering in trigonal systems is discussed in References 107 and 108.

In another work, Morimoto & Nagaosa (109) claimed that the electron correlation in multi-band systems can result in nonreciprocal I - V characteristics without time reversal symmetry breaking. According to this theoretical work, an analog of Onsager's relation shows that a nonreciprocal longitudinal current response without time reversal symmetry breaking generally requires two effects: dissipation and interactions (109). Nonreciprocity generally disappears without dissipation owing to the unitarity of the S -matrix, which describes the time evolution of the system (109). Nonreciprocal transport also requires interactions because time reversal symmetry results in symmetric band dispersion, which causes the symmetric transport response (109).

The effect of the geometry of the wave function on the second-order nonlinear current response along the transverse direction is also discussed in Reference 110. The second-order nonlinear current was derived as

$$j_a^{2\omega} = \frac{e^2}{2} \int_k \varepsilon_{abc} \Omega_b \varepsilon_c f_1^\omega - e \int_k f_2^{2\omega} \partial_a E(k), \quad 12.$$

where $E(k)$ is the energy dispersion; f_1^ω and $f_2^{2\omega}$ are the first- and second-order expansions of the electron distribution, respectively; and Ω_b , ε_c , and ε_{abc} represent the Berry curvature, electric field, and antisymmetric tensor, respectively. The second term vanishes under time reversal symmetry and the single τ approximation, and thus $j_a^{2\omega} = \chi_{abc} \varepsilon_b \varepsilon_c$, with

$$\chi_{abc} = -\varepsilon_{adc} \frac{e^3 \tau}{2(1+i\omega\tau)} \int_k f_0 (\partial_b \Omega_d) \equiv -\varepsilon_{adc} \frac{e^3 \tau}{2(1+i\omega\tau)} D_{bd}. \quad 13.$$

Here, D_{bd} represents the dipole moment of the Berry curvature in momentum space, which is called the Berry curvature dipole. The symmetry constraints of the finite Berry curvature dipole are discussed in Reference 111, and topological crystalline insulators, TMDs, and Weyl semimetals are proposed as potential candidates.

3.2. Experimental Observation of Nonlinear Hall Effect

The nonlinear anomalous Hall effect has been observed in WTe_2 , a semimetallic van der Waals crystal with strong spin-orbit interaction. The topology of the electronic band in monolayer or few-layer WTe_2 was studied, and electric-field-induced superconductivity in monolayer WTe_2 was even reported (28–30).

Ma et al. (112) fabricated a bilayer WTe_2 device with a dual-gate structure (**Figure 7a**) that affords separate control of both the carrier density and electrical displacement field D . Under the electrical displacement field, the only crystalline symmetry of bilayer WTe_2 is the mirror plane M_a , which allows the emergence of the nonlinear Hall effect originating from the Berry curvature dipole along the b direction (**Figures 7b** and **c**). Ma et al. measured the second harmonic voltage along several combinations and found that the nonlinear response can appear only along

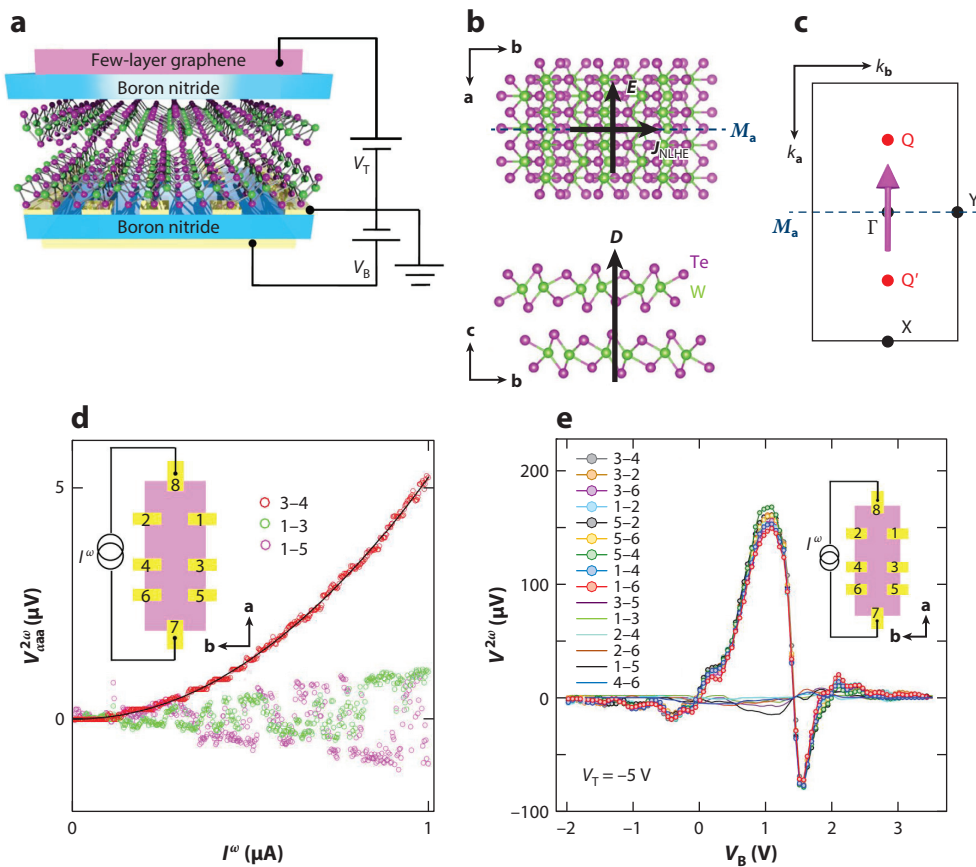


Figure 7

NLHE under time reversal symmetry in WTe₂. (a) Schematic of WTe₂ device. Carrier density and electrical displacement field D can be individually controlled by the dual-gate structure. (b) Symmetry of bilayer WTe₂ and selection rule of nonlinear transport. When an electric field is applied along the a direction, the nonlinear Hall response appears along the b direction, which is parallel to the mirror plane M_a . (c) Berry curvature dipole (arrow) in bilayer WTe₂. Dipole moment of the Berry curvature is perpendicular to the mirror plane. (d) Second harmonic resistance. Nonlinear voltage appears only along the transverse direction. (e) Gate dependence of the NLHE. The sign of the NLHE changes. Figure adapted from Reference 112 with permission. Abbreviation: NLHE, nonlinear Hall effect.

the transverse direction (Figure 7d), providing firm evidence of the nonlinear Hall effect under time reversal symmetry. In addition, they reported the characteristic sign reversal of the nonlinear Hall effect when the Fermi energy was changed (Figure 7e). The observed behaviors can be well explained by the theoretical calculations of the nonlinear Hall effect based on the Berry curvature dipole, further supporting their scenario.

The nonlinear anomalous Hall effect in few-layer WTe₂ was also reported by Kang et al. (113). In this work, in addition to the absence of the first harmonic voltage and the presence of the finite dc and second harmonic signals along the transverse direction, the authors measured the detailed angular dependence of the nonlinear anomalous Hall effect using a circular disc device. They interpreted the nonlinear Hall effect as the anomalous Hall effect owing to the current-induced magnetization and mentioned a possible scattering mechanism in addition to the intrinsic Berry curvature effect.

The nonlinear Hall effect is a new type of Hall effect that appears even under time reversal symmetry. Note that elucidation of the origin of the nonlinear Hall effect affords a deep understanding of the band topology/geometry or anomalous scattering mechanism. In the linear anomalous Hall effect, only the summation or the integral of the Berry curvature over the Brillouin zone (the Chern number, for example) is important. By contrast, for the nonlinear Hall effect, we must consider the detailed distribution of the Berry curvature (such as the Berry curvature dipole) or the directional dependence of the scattering.

The number of observations of nonlinear transport under time reversal symmetry to date is limited. The reason may be that the detailed directional dependence of the nonlinear transport is needed to identify nonlinear transport under time reversal symmetry. Experimental observation of the nonlinear longitudinal and Hall effect in other compounds under time reversal symmetry is highly desired, and their microscopic mechanisms should provide interesting insight into the physics of nonlinear responses in general.

4. BULK PHOTOVOLTAIC EFFECT

The bulk photovoltaic effect (114) is the emergence of a photoinduced spontaneous current in noncentrosymmetric crystals without a semiconductor p - n junction (115) or a bias voltage. It can generally be expressed as

$$j_i = \beta_{ijk} E_j E_k^*, \quad 14.$$

where E_j (E_k) is the electric field of the light for i (j) direction. According to Equation 14, the bulk photovoltaic effect can be understood as the second-order nonlinear current induced by the ac electric field of light. Like the nonlinear transport in response to a dc electric field, which was discussed in previous sections, the bulk photovoltaic effect is also attracting growing interest owing to its inherent quantum mechanical nature and intrinsic mechanism. In particular, the bulk photovoltaic effect was recently recognized as directly related to the band topology or geometry through the Berry curvature (dipole) or Berry connection (116–122). In this section, we review recent progress in experimental studies of the bulk photovoltaic effect in van der Waals nanostructures.

4.1. Bulk Photovoltaic Effect of Linearly Polarized Light

The photovoltaic effect induced by linearly polarized light is the counterpart of nonlinear dc transport under time reversal symmetry in the optical response. To date, it has been investigated in bulk polar crystals, including oxide materials (123–127), organic polar crystals (128), and halide compounds (129–132). These investigations suggested that polar symmetry plays a key role in the enhancement of the bulk photovoltaic effect, and the mechanism was discussed in terms of the quantum mechanical shift current. The shift current, which arises from the polarization current upon photoexcitation of polar materials, is one of the mechanisms of the photovoltaic effect. Because the polarization is characterized by the Berry connection, the shift current is quantified as the difference in Berry connection between the valence and conduction bands (120).

Among van der Waals materials, monolayer transition metal monochalcogenides were theoretically proposed as a candidate based on their in-plane polar structure (133, 134), which arises from the nonpolar bulk single crystals. This is an interesting feature of van der Waals nanostructures, where the symmetry is changed simply by the isolation of monolayers. However, the first experimental observation of the spontaneous photovoltaic effect in van der Waals materials was unexpectedly realized in TMD nanotube structures (**Figure 8a**; 135). The 2H-type monolayer

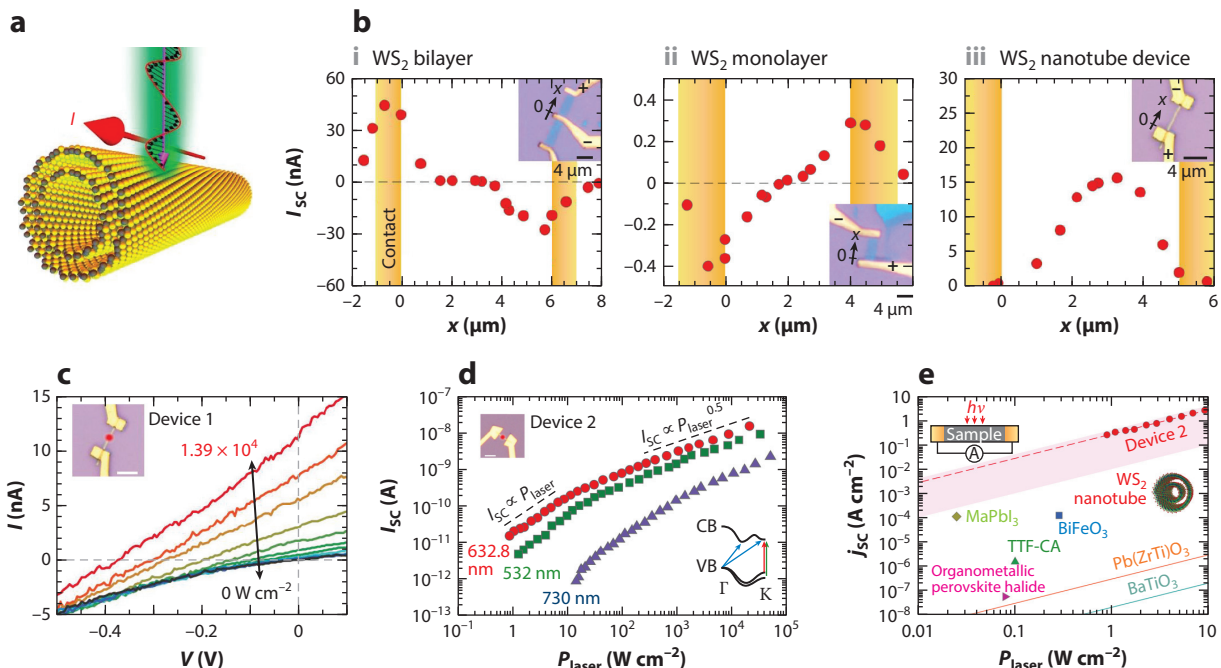


Figure 8

Large bulk photovoltaic effect in WS₂ nanotube. (a) Schematic of bulk photovoltaic effect in WS₂ nanotube. (b) Position-dependent photovoltaic response in WS₂ nanostructures with different symmetries. (i) Bilayer WS₂, (ii) monolayer WS₂, and (iii) WS₂ nanotube. In bilayer or monolayer WS₂, only the conventional Schottky barrier photovoltaic effect and/or the photothermal effect is observed when the laser spot illuminates the contact area. By contrast, a large bulk photovoltaic effect is observed at the center of the WS₂ nanotube. (c) I - V characteristics of WS₂ nanotube at different illumination intensities. (d) Power dependence of photocurrent at three wavelengths. I_{sc} shows a crossover from linear to square root behavior. (e) Bulk photovoltaic effect in various materials. The bulk photovoltaic effect in the WS₂ nanotube is an order of magnitude greater than those in the other materials. Inset shows the lateral geometry in which the effect was observed. Figure adapted from Reference 135 with permission. Abbreviations: CB, conduction band; TTF-CA, tetrathiafulvalene-*p*-chloranil; VB, valance band.

TMDs, for example, MoS₂ and WSe₂, are well known as materials with in-plane broken inversion symmetry, but they are not polar owing to their trigonal structure. When trigonal monolayers of TMDs or BN are rolled into tubular structures, they become polar along the tube direction (136). In fact, the photovoltaic effect in a BN nanotube was theoretically predicted in 2000 (137). This controllable structural symmetry is one of the most striking features of van der Waals nanostructures and led to the discovery of a large linear photovoltaic effect in a WS₂ nanotube (135).

Figure 8b shows the laser position dependence of the photoinduced short-circuit current (I_{sc}) in three types of WS₂ nanostructures with different crystal symmetry. For each device, the laser spot was scanned from one electrode to the other to distinguish the bulk photovoltaic effect from other effects such as the Schottky barrier photovoltaic effect or the photothermal effect near contacts (138). In bilayer WS₂ (**Figure 8b, subpanel i**), which has a centrosymmetric crystal structure, there is a finite photovoltaic response only when the contacts are illuminated by laser light, whereas no photocurrent signal is observed when the laser irradiates the flake itself. This behavior is consistent with the symmetry requirements for the bulk photovoltaic effect; i.e., inversion symmetry breaking is needed for the emergence of a photoinduced spontaneous

current. Although monolayer WS₂ has a noncentrosymmetric trigonal crystal structure, the result is similar to that of the bilayer device, which showed no notable photovoltaic response away from the contacts (**Figure 8b, subpanel ii**). I_{sc} also remains small when the laser spot is fixed near the center of the flake while the linear polarization direction is rotated. According to the symmetry argument, the photovoltaic effect can occur under light with linear polarization along the armchair direction. It seems that the amplitude of this bulk photovoltaic effect originating from trigonal symmetry is too small to observe and is buried within the photovoltaic response due to Schottky barriers and/or the photothermal effect.

In sharp contrast, I_{sc} increases significantly in the WS₂ nanotube device when the center of the nanotube is illuminated (**Figure 8b, subpanel iii**). The observed I_{sc} in the WS₂ nanotube (~ 15 nA) is orders of magnitude higher than that in the WS₂ monolayer (< 0.1 nA; **Figure 8b, subpanel ii**). This dramatic enhancement of I_{sc} away from the contacts in the nanotube device cannot be explained simply in terms of a difference in the amount of absorbed light, indicating that the reduction in crystal symmetry and the resulting polar symmetry are apparently crucial.

Figure 8c shows the I - V characteristics at various laser powers (P_{laser}). I_{sc} develops as the laser power increases. In **Figure 8d**, the laser power dependence of I_{sc} at laser wavelengths of 532, 632.8, and 730 nm is summarized in a log-log plot. Light with a wavelength of 632.8 nm (1.96 eV), which is nearly resonant with the A-exciton of WS₂, produces the strongest signal, indicating the effect of excitons on the bulk photovoltaic effect. In addition, **Figure 8d** provides an important insight into a possible mechanism of the bulk photovoltaic effect. It exhibits a crossover from a linear to a square root dependence near $P_{laser} = 10$ W/cm². This crossover is not expected to occur in the Schottky barrier photovoltaic effect at the interface of WS₂ and the metal contact, in which the photocurrent increases linearly even up to 5×10^3 W/cm² (139). Because the shift current model predicts this crossover from a linear to a square root dependence as a general feature caused by saturation of the carrier excitations (119), the shift current mechanism, among many possible mechanisms (140), may apply to the bulk photovoltaic effect in the WS₂ nanotube.

The observed strength of the bulk photovoltaic effect (the photocurrent density j_{sc}) in the WS₂ nanotube is compared with those in various materials in **Figure 8e**. For this comparison, only data acquired in a lateral geometry (**Figure 8e, inset**) were considered, because the device configuration strongly affects the device performance. The bulk photovoltaic effect is orders of magnitude larger in the WS₂ nanotube than in other bulk materials.

It is surprising that symmetry reduction in van der Waals nanostructures causes such a large effect. The availability of a simple strategy of symmetry engineering is a unique advantage of van der Waals nanostructures. In this case, nonpolar trigonal 2D crystals become polar when they form a nanotube, resulting in the modulation of the electronic states and the resulting electrical functionalities, including the photovoltaic response. Therefore, the above result offers an easy method of characterizing the symmetry of van der Waals nanostructures as well as the potential photovoltaic device applications of engineered van der Waals materials.

4.2. Circular Photovoltaic Effect

The circular photovoltaic effect consists of a photoinduced spontaneous current under circularly polarized light, where the sign of the photocurrent is opposite for right-handed and left-handed light. When it is accompanied by other effects, such as the bulk photovoltaic effect of linearly polarized light, the difference between the photocurrents under right-handed and left-handed light corresponds to the circular photovoltaic effect. Because circularly polarized light breaks time reversal symmetry, this effect is analogous to nonreciprocal transport with broken time reversal symmetry.

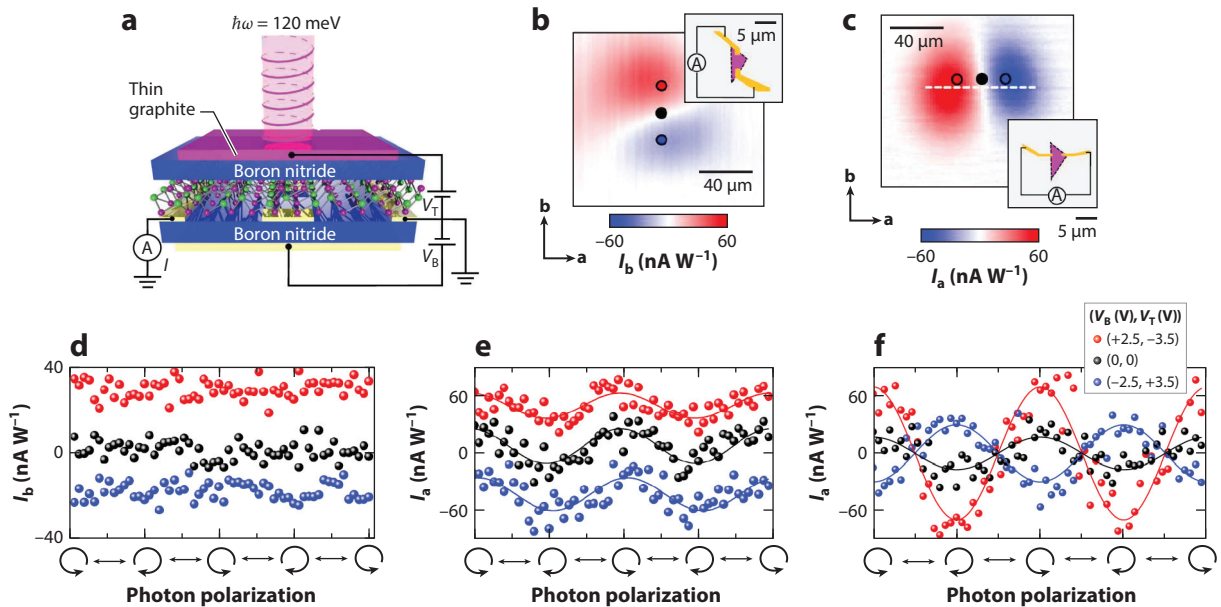


Figure 9

Circular photovoltaic effect in WTe_2 . (a) Schematic of photovoltaic effect in WTe_2 . (b) Photocurrent mapping along b axis under linearly polarized light. Bipolar spatial pattern due to the photothermal current is observed. (c) Photocurrent mapping along a axis. A bipolar spatial pattern similar to that in panel b is observed. (d) Polarization dependence of photovoltaic response along b axis. Red, black, and blue colors correspond to the positions in panel b . No circular photovoltaic effect is observed along the b axis. (e) Polarization dependence of photovoltaic response along a axis. Red, black, and blue colors correspond to the positions in panel c . Photocurrent shows modulation depending on the light polarization, clearly indicating the existence of the circular photovoltaic effect. (f) Electric field tuning of the circular photovoltaic effect. The sign reversal of the circular photovoltaic effect has been observed under an applied gate voltage, which can be explained in terms of Berry curvature dipole switching. Figure adapted from Reference 117 with permission.

The circular photovoltaic effect is generally observed at the interface, on the surface, or in the bulk polar material at oblique incidence (141–144). It is argued that a selective optical transition in the spin-splitting band caused by the circularly polarized light plays a key role in this effect.

However, the circular photovoltaic effect can be observed even under normal incidence; if there is only one mirror plane, circularly polarized light can generate a photocurrent perpendicular to the mirror plane. For example, this behavior was recently reported in WTe_2 (Figure 9a), where the topological origin of the circular photovoltaic effect was discussed and experimentally explored. In this experiment, Xu et al. (117) used mid-IR optoelectronic microscopy to optically excite electrons across the inverted quantum spin Hall gap and investigate the Berry curvature effect.

Figure 9b,c shows the photocurrent along the b and a directions, respectively, under linearly polarized light as a function of the beam spot position. In both cases, the sign of the photocurrent changes around the center of the device, producing bipolar spatial patterns. The sign change is attributed to the photothermal current, which originates from the difference in Seebeck coefficient between WTe_2 and the metal contacts. By contrast, the polarization dependence of the photocurrent along these two directions (Figure 9d,e) is quite different. The photocurrent along the a axis (Figure 9e) exhibits modulation depending on the polarization of the light. It is maximum for right-circularly polarized light, minimum for left-circularly polarized light, and zero

for linearly polarized light, clearly demonstrating the existence of the circular photovoltaic effect along the a axis. The photocurrent along the b axis does not exhibit this polarization dependence (**Figure 9d**), which is consistent with the symmetry. Furthermore, the sign reversal of the circular photovoltaic effect was observed under an applied gate voltage (**Figure 9f**). By theoretical considerations and band calculations, Xu et al. (117) explained the observed circular photovoltaic effect in terms of the Berry curvature dipole effect, which can be tuned electrically. A similar circular photovoltaic effect of topological origin has also been observed in the topological Weyl semimetal TaAs (118), and its relationship with the Weyl fermion chirality was discussed. In another recent work on chiral RhSi (119), the photon energy dependence of the circular photovoltaic effect was studied, and a significant enhancement of the circular photovoltaic effect was attributed to selective pumping of the Berry curvature monopole charge. Thus, the circular photovoltaic effect is becoming an important probe of the band topology/geometry in quantum materials.

5. SUMMARY AND OUTLOOK

In summary, we reviewed nonlinear electric transport originating from inversion symmetry breaking in van der Waals nanostructures. As demonstrated in the previous sections, nonlinear transport in solids is not only a unique functionality but also an important emerging probe of the characteristic electronic structure with a specific spin-orbit interaction or geometrical/topological properties, such as Berry connection or curvature, and unconventional pairing nature of superconductivity or vortex dynamics.

Because nonlinear transport is widely predicted in various quantum phases of noncentrosymmetric systems, the search for characteristic nonlinear transport reflecting the nature of each quantum phase is an important direction for future work. Typical examples include nonlinear electric transport in exotic quantum phases such as various types of topological semimetals, topological superconductors, and magnetic skyrmion systems. Exploring nonlinear transport with other origins, classifying the mechanisms, and understanding the relationship with electron correlation or dissipation are also important future endeavors.

In addition, nonlinear transport of uncharged particles or elementary excitations is another intriguing subject. In particular, the effects of symmetry breaking on phonon, magnon, and exciton transport are not well understood. The thermal and acoustic rectification effects or nonlinear spin or valley transport can be achieved in noncentrosymmetric systems, potentially providing an effective method of controlling energy quantum flows in solids.

Van der Waals nanostructures, in which we can freely design or control the symmetry, are an ideal material platform for studying such nonlinear transport. By exfoliating layered materials down to a monolayer or a few layers, or by applying an electric field at the surface, symmetry-reduced 2D systems can be easily obtained. Furthermore, van der Waals nanostructures such as nanotubes or hetero-/twisted interfaces have a unique symmetry, which is absent in bulk crystals. In some cases, in addition to the specific rotational or mirror symmetry, even translational symmetry is broken, providing a new opportunity for seeking novel quantum transport in solids. In addition to the second-order nonlinear transport, which is discussed in this review, higher-order nonlinear transport and other unprecedented types of quantum transport in van der Waals nanostructures should be explored in the future.

DISCLOSURE STATEMENT

The authors are not aware of any affiliations, memberships, funding, or financial holdings that might be perceived as affecting the objectivity of this review.

ACKNOWLEDGMENTS

We thank the following colleagues for their collaboration and discussions: Y. Tokura, N. Nagaosa, K. Hamamoto, S. Koshikawa, M. Ezawa, S. Shimizu, Y. Kaneko, F. Qin, W. Shi, M. Yoshida, A. Zak, R. Tenne, T. Kikitsu, D. Inoue, D. Hashizume, R. Wakatsuki, Y. Saito, S. Hoshino, Y.M. Itahashi, Y.J. Zhang, M. Onga, R. Suzuki, J.H. Smet, T. Nojima, and T. Morimoto.

We acknowledge financial support from the Japan Society for the Promotion of Science for a Grant-in-Aid for Scientific Research (S) (JP19H05602), the A3 Foresight Program, a Grant-in-Aid for Challenging Research (Exploratory) (JP19K21843), a Grant-in-Aid for Scientific Research (B) (JP19H01819), Grant-in-Aid for Scientific Research on Innovative Areas (JP20H05264), and the Japan Science and Technology (JST) Precursory Research for Embryonic Science and Technology (PRESTO) project (JPMJPR19L1).

LITERATURE CITED

1. Bauer E, Sigrist M, eds. 2012. *Non-centrosymmetric Superconductors: Introduction and Overview*. Berlin/Heidelberg: Springer-Verlag
2. Yip S. 2014. *Annu. Rev. Condens. Matter Phys.* 5:15–33
3. Bercioux D, Lucignano P. 2015. *Rep. Prog. Phys.* 78:106001
4. Bihlmayer G, Rader O, Winkler R. 2015. *New J. Phys.* 17:050202
5. Jia S, Xu SY, Hasan MZ. 2016. *Nat. Mater.* 15:1140–44
6. Yan B, Felser C. 2017. *Annu. Rev. Condens. Matter Phys.* 8:337–54
7. Burkov AA. 2018. *Annu. Rev. Condens. Matter Phys.* 9:359–78
8. Bell JS, Jackiw R. 1969. *Nuovo Cim. A* 60:47–61
9. Adler SL. 1969. *Phys. Rev.* 177:2426–38
10. Li Q, Kharzeev DE, Zhang C, Huang Y, Pletikoscic I, et al. 2016. *Nat. Phys.* 12:550–54
11. Xiong J, Kushwaha SK, Liang T, Krizan JW, Hirschberger M, et al. 2015. *Science* 350:413–16
12. Li H, He H, Lu HZ, Zhang H, Liu H, et al. 2016. *Nat. Commun.* 7:10301
13. Huang X, Zhao L, Long Y, Wang P, Chen D, et al. 2015. *Phys. Rev. X* 5:031023
14. Zhang CL, Xu SY, Belopolski I, Yuan Z, Lin Z, et al. 2016. *Nat. Commun.* 7:10735
15. Arnold F, Shekhar C, Wu SC, Sun Y, dos Reis RD, et al. 2016. *Nat. Commun.* 7:11615
16. Nagaosa N, Sinova J, Onoda S, MacDonald AH, Ong NP. 2010. *Rev. Mod. Phys.* 82:1539–92
17. Murakami S, Nagaosa N, Zhang SC. 2003. *Science* 301:1348–51
18. Kato YK, Myers RC, Gossard AC, Awschalom DD. 2004. *Science* 306:1910–13
19. Mak KF, McGill KL, Park J, McEuen PL. 2014. *Science* 344:1489–92
20. Onose Y, Ideue T, Katsura H, Shiomi Y, Nagaosa N, et al. 2010. *Science* 329:297–99
21. Ideue T, Onose Y, Katsura H, Shiomi Y, Ishiwata S, et al. 2012. *Phys. Rev. B* 85:134411
22. Ideue T, Kurumaji T, Ishiwata S, Tokura Y. 2017. *Nat. Mater.* 16:797–802
23. Onga M, Zhang Y, Ideue T, Iwasa Y. 2017. *Nat. Mater.* 16:1193–97
24. Tokura Y, Nagaosa N. 2018. *Nat. Commun.* 9:340
25. Castro Neto AH, Guinea F, Peres NMR, Novoselov KS, Geim AK. 2009. *Rev. Mod. Phys.* 81:109–62
26. Xu X, Yao W, Xiao D, Heinz TF. 2014. *Nat. Phys.* 10:343–50
27. Saito Y, Nojima T, Iwasa Y. 2016. *Nat. Rev. Mater.* 2:16094
28. Fei Z, Palomaki T, Wu S, Zhao W, Cai X, et al. 2017. *Nat. Phys.* 13:677–82
29. Tang S, Zhang C, Wong D, Pedramrazi Z, Tsai H-Z, et al. 2017. *Nat. Phys.* 13:683–87
30. Fatemi V, Wu S, Cao Y, Bretheau L, Gibson QD, et al. 2018. *Science* 362:926–29
31. Gong C, Li L, Li Z, Ji H, Stern A, et al. 2017. *Nature* 546:265–69
32. Huang B, Clark G, Navarro-Moratalla E, Klein DR, Cheng R, et al. 2017. *Nature* 546:270–73
33. Charlier JC, Blase X, Roche S. 2007. *Rev. Mod. Phys.* 79:677–732
34. Laird EA, Kuemmeth F, Steele GA, Grove-Rasmussen K, Nygård J, et al. 2015. *Rev. Mod. Phys.* 87:703–64
35. Geim AK, Grigorieva IV. 2013. *Nature* 499:419–25

36. Lee CH, Lee GH, van der Zande AM, Chen W, Li Y, et al. 2014. *Nat. Nanotechnol.* 9:676–81
37. Britnell L, Gorbachev RV, Jalil R, Belle BD, Schedin F, et al. 2012. *Science* 335:947–50
38. Song T, Cai X, Matisse W-YT, Zhang X, Huang B, et al. 2018. *Science* 360:1214–18
39. Yankowitz M, Xue J, Cormode D, Sanchez-Yamagishi JD, Watanabe K, et al. 2012. *Nat. Phys.* 8:382–86
40. Dean CR, Wang L, Maher P, Forsythe C, Ghahari F, et al. 2013. *Nature* 497:598–602
41. Cao Y, Fatemi V, Demir A, Fang S, Spencer L, et al. 2018. *Nature* 556:80–84
42. Cao Y, Fatemi V, Fang S, Watanabe K, Taniguchi T, et al. 2018. *Nature* 556:43–50
43. Seyler KL, Rivera P, Yu H, Wilson NP, Ray EL, et al. 2019. *Nature* 567:66–70
44. Tran K, Moody G, Wu F, Lu X, Choi J, et al. 2019. *Nature* 567:71–75
45. Jin C, Regan EC, Yan A, Utama MIB, Wang D, et al. 2019. *Nature* 567:76–80
46. Liu Y, Rodrigues JNB, Luo YZ, Li L, Yang ACM, et al. 2018. *Nat. Nanotechnol.* 13:828–34
47. Rikken GLJA, Fölling J, Wyder P. 2001. *Phys. Rev. Lett.* 87:236602
48. Krstić V, Roth S, Burghard M, Kern K, Rikken GLJA. 2002. *J. Chem. Phys.* 117:11315–19
49. Pop F, Auban-Senzier P, Canadell E, Rikken GLJA. 2014. *Nat. Commun.* 5:3757
50. Rikken GLJA, Wyder P. 2005. *Phys. Rev. Lett.* 94:016601
51. Olejník K, Novák V, Wunderlich J, Junwirth T. 2015. *Phys. Rev. B* 91(18):180402
52. Avci CO, Garello K, Ghosh A, Gabureac M, Alvarado SF, et al. 2015. *Nat. Phys.* 11:570–75
53. Yasuda K, Tsukazaki A, Yoshimi R, Takahashi KS, Kawasaki M, et al. 2016. *Phys. Rev. Lett.* 117:127202
54. He P, Zhang SSL, Zhu D, Liu Y, Wang Y, et al. 2018. *Nat. Phys.* 14:495–99
55. He P, Walker SM, Zhang SSL, Bruno FY, Baharamy MS, et al. 2018. *Phys. Rev. Lett.* 120:266802
56. Choe D, Jin M-J, Kim S-I, Choi H-J, Jo J, et al. 2019. *Nat. Commun.* 10:4510
57. Guillet T, Zucchetti C, Barbedienne Q, Marty A, Isella G, et al. 2020. *Phys. Rev. Lett.* 124:027201
58. Lustikova J, Shiomi Y, Yokoi N, Kabeya N, Kimura N, et al. 2018. *Nat. Commun.* 9:4922
59. Yasuda K, Yasuda H, Liang T, Yoshimi R, Tsukazaki A, et al. 2019. *Nat. Commun.* 10:2734
60. Itahashi YM, Ideue T, Saito Y, Shimizu S, Ouchi T, et al. 2020. *Sci. Adv.* 6:eay9120
61. Ideue T, Hamamoto K, Koshikawa S, Ezawa M, Shimizu S, et al. 2017. *Nat. Phys.* 13:578–83
62. He P, Hsu CH, Shi S, Cai K, Wang J, et al. 2019. *Nat. Commun.* 10:1290
63. Ishizaka K, Baharamy MS, Murakawa H, Sakano M, Shimojima T, et al. 2011. *Nat. Mater.* 10:521–26
64. Sakano M, Baharamy MS, Katayama A, Shimojima T, Murakawa H, et al. 2013. *Phys. Rev. Lett.* 110:107204
65. Murakawa H, Baharamy MS, Tokunaga M, Kohama Y, Bell C, et al. 2013. *Science* 342:1490–93
66. Ideue T, Checkelsky JG, Murakawa H, Baharamy MS, Kaneko Y, et al. 2014. *Phys. Rev. B* 90:161107(R)
67. Ideue T, Ye L, Checkelsky JG, Murakawa H, Kaneko Y, et al. 2015. *Phys. Rev. B* 92:115144
68. Wang QH, Kalantar-Zadeh K, Kis A, Coleman JN, Strano MS. 2012. *Nat. Nanotechnol.* 7:699–712
69. Mak KF, Shan J. 2016. *Nat. Photonics* 10:216–26
70. Zhu ZY, Cheng YC, Schwingenschlögl U. 2011. *Phys. Rev. B* 84:153402
71. Xiao D, Liu GB, Feng W, Xu X, Yao W. 2010. *Phys. Rev. Lett.* 108:196802
72. Bisri SZ, Shimizu S, Nakano M, Iwasa Y. 2017. *Adv. Mater.* 29:1607054
73. Ueno K, Nakamura S, Shimotani H, Ohtomo A, Kumura N, et al. 2008. *Nat. Mater.* 7:855–58
74. Ueno K, Nakamura S, Shimotani H, Yuan HT, Kumura N, et al. 2011. *Nat. Nanotechnol.* 6:408–12
75. Ye JT, Zhang YJ, Akashi R, Bahramy MS, Arita R, et al. 2012. *Science* 338:1193–96
76. Saito Y, Nakamura Y, Bahramy MS, Kohama Y, Ye J, et al. 2016. *Nat. Phys.* 12:144–49
77. Lu JM, Zheliuk O, Leermakers I, Yuan NFQ, Zeitler U, et al. 2015. *Science* 350:1353–57
78. Xi X, Wang Z, Zhao W, Park JH, Law KT, et al. 2016. *Nat. Phys.* 12:139–43
79. Wakatsuki R, Saito Y, Hoshino S, Itahashi YM, Ideue T, et al. 2017. *Sci. Adv.* 3:e1602390
80. Liu GB, Shan WY, Yao Y, Yao W, Xiao D. 2013. *Phys. Rev. B* 88:085433
81. Kormányos A, Zólyomi V, Drummond ND, Rakyta P, Burkard G, et al. 2013. *Phys. Rev. B* 88:045416
82. Wakatsuki R, Nagaosa N. 2018. *Phys. Rev. Lett.* 121:026601
83. Saito Y, Kasahara Y, Ye J, Iwasa Y, Nojima T. 2015. *Science* 350:409–13
84. Tsen AW, Hunt B, Kim YD, Yuan ZJ, Jia S, et al. 2016. *Nat. Phys.* 12:208–12
85. Kapitlnik A, Kivelson SA, Spivak B. 2019. *Rev. Mod. Phys.* 91:011002
86. Itahashi YM, Saito Y, Ideue T, Nojima T, Iwasa Y. 2020. *Phys. Rev. Res.* 2:023127

87. Hoshino S, Wakatsuki R, Hamamoto K, Nagaosa N. 2018. *Phys. Rev. B* 98:054510
88. Villegas JE, Savel S, Nori F, Gonzalez EM. 2003. *Science* 302:1188–91
89. Villegas JE, Gonzalez EM, Gonzalez MP, Anguita JV, Vicent JL. 2005. *Phys. Rev. B* 71:24519
90. de Souza Silva CC, Van de Vondel J, Morelle M, Moshchalkov VV. 2006. *Nature* 440:651–54
91. Lu Q, Reichhardt CJO, Reichhardt C. 2007. *Phys. Rev. B* 75:054502
92. Kato A, Tanimura Y. 2013. *J. Phys. Chem. B* 117:13132–44
93. Hamamoto K, Park T, Ishizuka H, Nagaosa N. 2019. *Phys. Rev. B* 99:064307
94. Yokouchi T, Hoshino S, Kanazawa N, Kikkawa A, Morikawa D, et al. 2018. *Sci. Adv.* 4:eaat115
95. Aoki R, Kousaka Y, Togawa Y. 2019. *Phys. Rev. Lett.* 122:057206
96. Rikken GLJA, Avarvari N. 2019. *Phys. Rev. B* 99:245153
97. Ideue T, Hirayama M, Taiko H, Takahashi T, Murase M, et al. 2019. *PNAS* 116:25530–34
98. Sakano M, Hirayama M, Takahashi T, Akebi S, Nakayama M, et al. 2020. *Phys. Rev. Lett.* 124:136404
99. Qin F, Shi W, Ideue T, Yoshida M, Zak A, et al. 2017. *Nat. Commun.* 8:14465
100. Qin F, Ideue T, Shi W, Zhang X, Yoshida M, et al. 2018. *Nano Lett.* 18:6789–94
101. Tenne R, Marguils L, Genut M, Hodes G. 1992. *Nature* 360:444–60
102. Rothschild A, Sloan J, Tenne R. 2000. *J. Am. Chem. Soc.* 122:5169–79
103. Zak A, Sallacan-Ecker L, Margolin A, Feldman Y, Popovitz-Biro R, et al. 2010. *Fullerene, Nanotubes, Carbon Nanostruct.* 19:18–26
104. Shi W, Ye J, Zhang Y, Suzuki R, Yoshida M, et al. 2015. *Sci. Rep.* 5:12534
105. Qin F, Ideue T, Shi W, Zhang Y, Suzuki R, et al. 2018. *J. Vis. Exp.* 134:e56862
106. Little WA, Parks RD. 1962. *Phys. Rev. Lett.* 9:9–12
107. Yu H, Wu Y, Liu GB, Xu X, Yao W. 2014. *Phys. Rev. Lett.* 113:156603
108. Isobe H, Xu SY, Fu L. 2020. *Sci. Adv.* 6:eaay2497
109. Morimoto T, Nagaosa N. 2018. *Sci. Rep.* 8:2973
110. Sodemann I, Fu L. 2015. *Phys. Rev. Lett.* 115:21806
111. Zhang Y, Sun Y, Yan B. 2018. *Phys. Rev. B* 97:041101(R)
112. Ma Q, Xu SY, Shen H, MacNeill D, Fatemi V, et al. 2019. *Nature* 565:337–42
113. Kang K, Li T, Sohn E, Shan J, Mak KF. 2019. *Nat. Mater.* 18:324–28
114. Sturman BI, Fridkin VM. 1992. *The Photovoltaic and Photorefractive Effects in Noncentrosymmetric Materials*. Philadelphia, PA: Gordon and Breach Sci. Publ.
115. Shockley W. 1949. *AT&T Tech. J.* 28:435–89
116. Ma Q, Xu SY, Chan CK, Zhang CL, Chang G, et al. 2017. *Nat. Phys.* 13:842–47
117. Xu SY, Ma Q, Shen H, Fatemi V, Wu S, et al. 2018. *Nat. Phys.* 14:900–6
118. Osterhoudt GB, Diebel LK, Gray MJ, Yang X, Stanco J, et al. 2019. *Nat. Mater.* 18:471–75
119. Rees D, Manna K, Lu B, Morimoto T, Borrmann H, et al. 2020. *Sci. Adv.* 6:eaba0509
120. Morimoto T, Nagaosa N. 2016. *Sci. Adv.* 2:e1501524
121. Juan F, Grushin AG, Morimoto T, Morre JE. 2017. *Nat. Commun.* 8:15995
122. Fregoso BM, Morimoto T, Moore JE. 2017. *Phys. Rev. B* 96:075421
123. Grinberg I, West DV, Torres M, Gou G, Stein DM, et al. 2013. *Nature* 503:509–12
124. Brody PS. 1975. *J. Solid State Chem.* 12:193–200
125. Yang SY, Seidel J, Byrnes SJ, Shafer P, Yang CH, et al. 2010. *Nat. Nanotechnol.* 5:143–47
126. Nechache R, Harnagea C, Licoccia S, Traversa E, Ruediger A, et al. 2011. *Appl. Phys. Lett.* 98:202902
127. Nakamura M, Kagawa F, Tanigaki T, Park HS, Matsuda T, et al. 2016. *Phys. Rev. Lett.* 116:156801
128. Nakamura M, Horiuchi S, Kagawa F, Ogawa N, Kurumaji T, et al. 2017. *Nat. Commun.* 8:281
129. Xiao Z, Yuan Y, Shao Y, Wang Q, Dong Q, et al. 2015. *Nat. Mater.* 14:193–98
130. Sun Z, Liu X, Khan T, Ji C, Asghar MA, et al. *Angew. Chem., Int. Ed.* 55:6545–50
131. Ogawa N, Sotome M, Kaneko Y, Ogino M, Tokura Y. 2017. *Phys. Rev. B* 96:241203
132. Sotome M, Nakamura M, Fujioka J, Ogino M, Kaneko Y, et al. 2019. *PNAS* 116:1929–33
133. Cook AM, Fregoso BM, Juan F, Coh S, Moore JE. 2017. *Nat. Commun.* 8:14176
134. Rangel T, Fregoso BM, Mendoza BS, Morimoto T, Moore JE, et al. 2017. *Phys. Rev. Lett.* 119:067402
135. Zhang YJ, Ideue T, Onga M, Qin F, Suzuki R, et al. 2019. *Nature* 570:349–53
136. Nakhmanson SM, Calzolari A, Meunier V, Bernholc J, Nardelli MB. 2003. *Phys. Rev. B* 67:235406

137. Kral P, Mele EJ, Tomanek D. 2000. *Phys. Rev. Lett.* 85:1512–15
138. Tauc J. 1957. *Rev. Mod. Phys.* 29:308–24
139. Zhang C, Wang S, Yang L, Liu Y, Xu T, et al. 2012. *Appl. Phys. Lett.* 100:243101
140. Yuan YB, Xiao ZG, Yang B, Huang JS. 2014. *J. Mater. Chem. A* 2:6027–41
141. Yuan H, Wang X, Lian B, Zhang H, Fang X, et al. 2014. *Nat. Nanotechnol.* 9:851–57
142. Ogawa N, Baharamy MS, Kaneko Y, Tokura Y. 2014. *Phys. Rev. B* 90:125122
143. Okada KN, Ogawa N, Yoshimi R, Tsukazaki A, Takahashi KS. 2016. *Phys. Rev. B* 93:081403
144. Ganichev SD, Prettl W. 2003. *J. Phys. Condens. Matter* 15:R935–83



Contents

Have I Really Been a Condensed Matter Theorist? I'm Not Sure, but Does It Matter? <i>Edouard Brézin</i>	1
A Career in Physics <i>Bertrand I. Halperin</i>	15
Mechanical Frequency Tuning by Sensory Hair Cells, the Receptors and Amplifiers of the Inner Ear <i>Pascal Martin and A.J. Hudspeth</i>	29
On the Role of Competing Interactions in Charged Colloids with Short-Range Attraction <i>José Ruiz-Franco and Emanuela Zaccarelli</i>	51
The Fracture of Highly Deformable Soft Materials: A Tale of Two Length Scales <i>Rong Long, Chung-Yuen Hui, Jian Ping Gong, and Eran Bouchbinder</i>	71
Modeling Grain Boundaries in Polycrystalline Halide Perovskite Solar Cells <i>Ji-Sang Park and Aron Walsh</i>	95
Creep Motion of Elastic Interfaces Driven in a Disordered Landscape <i>Ezequiel E. Ferrero, Laura Foini, Thierry Giamarchi, Alejandro B. Kolton, and Alberto Rosso</i>	111
Stem Cell Populations as Self-Renewing Many-Particle Systems <i>David J. Jörg, Yu Kitadate, Shosei Yoshida, and Benjamin D. Simons</i>	135
Polyelectrolyte Complex Coacervates: Recent Developments and New Frontiers <i>Artem M. Rumyantsev, Nicholas E. Jackson, and Juan J. de Pablo</i>	155
Enzymes as Active Matter <i>Subhadip Ghosh, Ambika Somasundar, and Ayusman Sen</i>	177
Symmetry Breaking and Nonlinear Electric Transport in van der Waals Nanostructures <i>Toshiya Ideue and Yoshihiro Iwasa</i>	201

Band Representations and Topological Quantum Chemistry <i>Jennifer Cano and Barry Bradlyn</i>	225
Topology and Symmetry of Quantum Materials via Nonlinear Optical Responses <i>J. Orenstein, J.E. Moore, T. Morimoto, D.H. Torchinsky, J.W. Harter, and D. Hsieh</i>	247
Organization and Self-Assembly Away from Equilibrium: Toward Thermodynamic Design Principles <i>Michael Nguyen, Yuqing Qiu, and Suriyanarayanan Vaikuntanathan</i>	273

Errata

An online log of corrections to *Annual Review of Condensed Matter Physics* articles may be found at <http://www.annualreviews.org/errata/conmatphys>